OVERLAY

Journal of Theoretical, Computational and Applied Mechanics

JTCAM

DIAMOND OPEN ACCESS

Identifiers
DOI 10.46298/jtcam.11335
HAL hal-04100630v3

History
Received May 19, 2023
Accepted Dec 20, 2023
Published Sept 26, 2024

Associate Editor
Anna Pandolfi

Reviewers
Luca Andena
Anonymous

Open Review
HAL hal-04614645

Supplementary Material
Data
DOI 10.5281/zenodo.13788675

Licence
CC BY 4.0
©The Authors

Deformation and cavitation at the spherulite scale of an isotactic polypropylene

Lucien Laiarinandrasana[1], Olga Klinkova[2], Cristian Ovalle[1], Peter Cloetens[3], Henry Proudhon[1], and Thilo F. Morgeneyer[1]

[1] Mines Paris, PSL University, Centre for Material Sciences, UMR7633 CNRS, Evry, France
[2] Quartz Laboratory EA7393, ISAE-Supméca, Saint-Ouen, France
[3] European Synchrotron Radiation Facility, Grenoble, France

Engineering stress-strain curves are generated from tensile tests on semi-crystalline thermoplastics, which may exhibit non-linearity and/or peak stress associated with striction/necking phenomenon of the specimen at the macroscopic scale. This work addresses this state of deformed specimen, on an isotactic polypropylene, where irreversible strains have led to a variable cross-sectional area along the necked region. 3D images in this region, obtained through Synchrotron Radiation Computed Tomography with two high resolutions are exploited. The best resolution (1 pixel length = 0.05 µm) allowed a better understanding of the morphology of several deformed spherulites within which polar fan arrangements are clearly detailed. Thanks to the identification of the boundaries of spherulite patterns, with a 0.7 µm resolution, the longitudinal and transverse elongations of larger numbers of spherulites are measured. The evolution of the volumetric plastic strains due to cavitation at the spherulitic scale along the necked regions is comprehensively analysed. Volume changes at this scale are highlighted, consisting of an increase in the case of void growth followed by a decrease at large strains due to the collapse of elongated voids. The effects of these results on the establishment of reliable constitutive model are discussed. It is found that accounting for plastic dilation is necessary for the accuracy of constitutive models.

Keywords: semi-crystalline polymer, spherulite, cavitation, deformation, tomography

1 Introduction

Present day requirements for sustainability within a circular economy encourage the use of thermoplastic materials for engineering structures and is one of the recommended solutions due to their recyclability. To this end, investigation of the mechanical properties of these materials is a key point, whatever their origin: recycled or as initially processed.

This work focuses on an isotactic polypropylene: a semi-crystalline thermoplastic with a spherulitic microstructure (Laiarinandrasana, Selles, et al. 2016). The aim is to relate the evolution of the microstructure, analysed from 3D imaging techniques, in terms of mechanisms of deformation and voiding, to the mechanical property allowing the constitutive relationships of the material to be established. The most common mechanical test dedicated to analyse the mechanical behaviour of a given material consists of a tensile loading applied to a uniaxial specimen. Generally, during such a test, a change in the specimen morphology (noted as necking or striction) (Ward 1971; Duffo et al. 1995; Séguéla 2007) appears around the yield stress. This localisation of the deformation obviously introduces a heterogeneity within the gauge length of the specimen which is accompanied by a change in the slope of the engineering stress-strain curve: non-linearity, peak stress… This latter property is considered to be a manifestation at the macroscopic scale of a profound change at the microstructure scale (Blaise et al. 2010).

The spherulitic microstructure in its undeformed configuration (initial microstructure) is usually examined in two dimensions (Haudin 2013; Laiarinandrasana, Selles, et al. 2016), so as to evaluate the average diameter of the spherulites. However, the tomography technique, especially

Synchrotron Radiation Computed Tomography (SRCT) extended these examinations to three dimensions. One of the noticeable results (Selles et al. 2017; Raphael et al. 2019) concerned 3D deformed spherulite in Polyamide 6, where the existence of a cylindrical nucleus in the centre was mentioned. Moreover, quantitative evaluation of the void volume fraction (porosity) through the thickness of smooth and notched round bars was performed by Laiarinandrasana, Selles, et al. (2016). It was mentioned that whilst the spherulite axial deformation could easily be estimated by measuring the height of the polar fans (Pawlak et al. 2008; Pawlak et al. 2010) in the tensile direction, the radial deformation was difficult to evaluate without a clear identification of the lateral boundary of these spherulites. Hence, this is the first objective of this paper, which could be attempted thanks to available SRCT data sets at two resolutions. A very good resolution at 0.05 µm allowed the identification of 3D patterns of deformed shape of spherulites. A lower resolution of 0.7 µm permitted more spherulites to be analysed. Histograms of the height and the diameter of these spherulites were then plotted.

The application of the continuum mechanics theory is based on the existence of a representative volume element (RVE). Laiarinandrasana, Selles, et al. (2016) mentioned that the initial rectangular cross-section of the polypropylene under study became diamond like shaped during tensile deformation. Indeed, warping of the side of the cross-section was systematically observed in 3D. After a clear definition of the RVE corresponding to the spherulitic microstructure, the effect of the aforementioned warping of the sides of the cross-section was also investigated.

Addressing the mechanical properties, many attempts have been made to access the local stress (Xiong et al. 2013) within the spherulite, by using the continuum mechanics framework. However, the only measurement available was the resulting force provided by the load cell, *i.e.* at the macroscopic scale. The redistribution of this load to the three main directions of the space was guessed to be due to the microstructure. Therefore, estimating the local stresses requires a reliable constitutive model which should be, at least, based on the strain measurements at the scale of the spherulite as mentioned above. In the literature, several models have been proposed for homogenised spherulites taken beyond the yield stress, *i.e.* during the necking process. The "plastic dilation" was taken into account by introducing the porosity as an internal variable in an approach using the mechanics of porous media, see (Ognedal et al. 2014; Laiarinandrasana, Klinkova, et al. 2016) and references therein. Other models broke the homogenisation assumption by considering an intrinsic stress-strain curve (Duffo et al. 1995; Estevez et al. 2000; Addiego et al. 2006; Ponçot et al. 2013), clearly related to the matrix with no voids, that is, responding to the deviatoric part of the stress and strain tensors. Several models even go further by distinguishing the crystalline and amorphous lamellae with their specific orientations inside the spherulite (van Dommelen et al. 2003), but without any mention of the voids observed in the spherulites considered.

This paper aimed at shedding light on the aforementioned concepts. It starts with a background, first, of the idealised deformed spherulite with the voids inside, then, of the continuum mechanics using the framework of total Lagrange finite strain formulation. The deformation gradient tensor will be considered as the input of the problem. The second section describes the investigated material together with the working methods and the available tomographic data sets. The following section details the experimental results allowing the deformation gradient tensor to be obtained at three various scales, implying therefore, three RVEs. In the last part, a discussion proposes the physical mechanisms underlying the deformation gradient components, in 3D, as well as the relevant constitutive models able to account for these mechanisms. This section ends by a short comment about the possible use of machine learning approach to handle big data available in the laboratory.

2 Background

2.1 Voiding inside a spherulite

When semi-crystalline polymers have experienced yielding during tensile tests, microstructural changes were reported to occur (Blaise et al. 2010; Ovalle et al. 2021). The examinations of these microstructure modifications were performed when the specimen was stress-free. Therefore, the

observed deformation was irreversible. In the following work, attention is paid on the appearance of polar fans (Pawlak et al. 2008; Pawlak et al. 2010; Selles et al. 2017). Whereas the polar fans were reported to develop inside a spherulite, their characterisation in terms of size, morphology and dispersion has been studied (Laiarinandrasana, Klinkova, et al. 2016; Laiarinandrasana, Selles, et al. 2016):

- on a volume of interest larger than the size of one spherulite. Typically, voids were reported to be cylindrical, and their volume fraction exhibited a gradient showing a maximum located in the centre of the specimen;
- with increasing deformation involving a change in the neck shape. The growth of initially penny shaped voids was described as follows:
  - during the stress-softening stage, the height increased without any change in the diameter;
  - at the beginning of the stress plateau until failure, the height was still increasing but the diameter diminished. This latter result was due to void coalescence in both the radial and in column directions (Laiarinandrasana, Selles, et al. 2016). At the end of this process, the collapse of many cylindrical voids can be observed ;
  - before the failure, the diameter is stabilised (complete collapse of the voids) and the evolution of the height can no longer be observed.

In addition to polar fans development, equatorial dispersed voids appeared during the stress-softening (Selles et al. 2017). Their specificity was to keep penny shape morphology, exhibiting rather radial extension and even coalescence, and not much increase in height.

In a previous study, Laiarinandrasana, Selles, et al. (2016) analysed two semi-crystalline polymers: an isotactic polypropylene and a polyamide 6 using, respectively, flat geometries showing a marked microstructural skin-core effect and homogeneous round bars. Both samples were tested in tension until a small extension of necking. Then, tomography technique allowed the *ex-situ* observations of voids appearing within spherulites in the form of two symmetrical fans, one at each end of the spherulites. A full study of the voids in these polar fans has been carried out in terms of morphology, general arrangement and characteristic length.

Furthermore, according to (Selles et al. 2017; Raphael et al. 2019; Pawlak et al. 2008; Pawlak et al. 2010), a deformed spherulite reveals:

- a nucleus without voiding located in the central part;
- polar fans constituted by penny shaped voids arranged in columns along the tensile direction. Polymer matrix can still be observed between two voids;
- equatorial voids considered located at a plane perpendicular to the tensile direction. The presence of the nucleus means that only a ring-shaped void can be considered.

Figure 1 shows an idealised deformed spherulite containing the above-mentioned elements. As 3D concepts will be discussed, a perspective view is proposed in Figure 1(a) where the tensile direction is represented by a black arrow. The boundary of the spherulite is ideally considered as ellipsoidal and drawn with a dashed black line. The north polar fan (supposed to be related to the North Pole) is indicated in this sketch. It contains three penny-shaped voids with increasing diameters when approaching the North Pole. In the centre of the spherulite, the nucleus is represented as a white cylinder. This nucleus is surrounded by the ring of equatorial voids. 2D views of this sketch are represented in Figure 1(b), where the cylindrical coordinates are illustrated at the bottom: z direction coinciding with the tensile axis. The cut following the (r, z) plane will be assigned to the "side view", whereas the (r, θ) plane will be supposed to be a "top view". In the top part of Figure 1(b), a specific top view related to a cross-sectional cut of the spherulite at the second void in the North polar fan is illustrated. The grey radial stripes are supposed to illustrate the lamellae. It should be mentioned that if the cut is operated in-between two voids, only a plain circle with grey rays could be seen (no void in the polar fan). In the following, the essential of the work will be carried out on 2D sections of 3D images. The sketches in Figure 1(b) should be kept in mind for the interpretation.

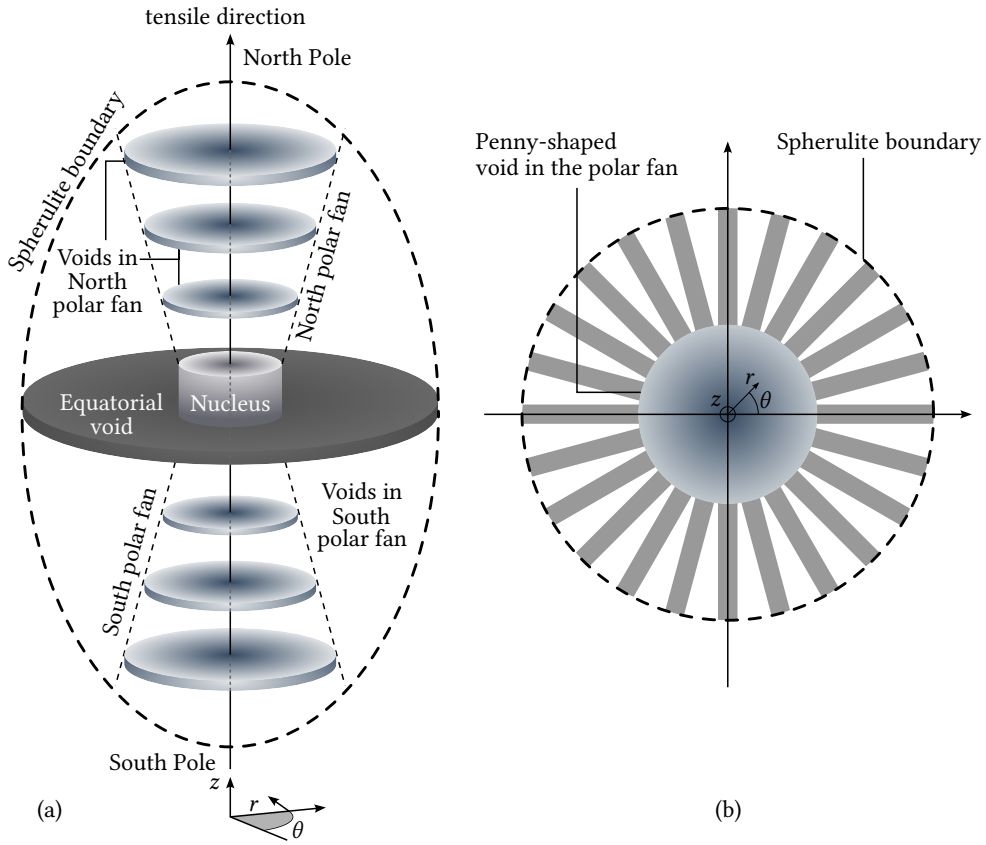

Figure 1 Idealised views of a deformed spherulite: (a) perspective view in 3D; (b) 2D view from the cross-section cut (top view). Cylindrical coordinates are shown under the South Pole.

2.2 Finite strain formulations

In the framework of finite strain under total Lagrangian formulation, let

$$\underset{\sim}{F} = \begin{pmatrix} \lambda_r & 0 & 0 \\ 0 & \lambda_\theta & 0 \\ 0 & 0 & \lambda_z \end{pmatrix} \tag{1}$$

be the deformation gradient in a cylindrical system of coordinates, with z being the tensile direction. In the whole document, isotropy of the material is assumed, so that $\lambda_r = \lambda_\theta$. Therefore, only two elongations will be considered:

- the longitudinal elongation λ_L which is equal to λ_z,
- the transverse elongation $\lambda_T = \lambda_r = \lambda_\theta$.

The simplified deformation gradient tensor which will be referred to in the following, becomes

$$\underset{\sim}{F} = \begin{pmatrix} \lambda_T & 0 & 0 \\ 0 & \lambda_T & 0 \\ 0 & 0 & \lambda_L \end{pmatrix}. \tag{2}$$

The classical multiplicative decomposition of $\underset{\sim}{F}$ reads

$$\underset{\sim}{F} = \underset{\sim}{F}^{\,\mathrm{e}}\,\underset{\sim}{F}^{\,\mathrm{p}} = \begin{pmatrix} \lambda_T^{\mathrm{e}}\lambda_T^{\mathrm{p}} & 0 & 0 \\ 0 & \lambda_T^{\mathrm{e}}\lambda_T^{\mathrm{p}} & 0 \\ 0 & 0 & \lambda_L^{\mathrm{e}}\lambda_L^{\mathrm{p}} \end{pmatrix} \tag{3}$$

where superscripts ‘e’ and ‘p’ stand respectively for elastic and plastic components. By using the logarithmic true strain measure, the strain tensor

$$\underset{\sim}{\varepsilon} = \begin{pmatrix} \varepsilon_T = \ln(\lambda_T^{\mathrm{e}}\lambda_T^{\mathrm{p}}) & 0 & 0 \\ 0 & \varepsilon_T = \ln(\lambda_T^{\mathrm{e}}\lambda_T^{\mathrm{p}}) & 0 \\ 0 & 0 & \varepsilon_L = \ln(\lambda_L^{\mathrm{e}}\lambda_L^{\mathrm{p}}) \end{pmatrix} = \begin{pmatrix} \varepsilon_T^{\mathrm{e}} + \varepsilon_T^{\mathrm{p}} & 0 & 0 \\ 0 & \varepsilon_T^{\mathrm{e}} + \varepsilon_T^{\mathrm{p}} & 0 \\ 0 & 0 & \varepsilon_L^{\mathrm{e}} + \varepsilon_L^{\mathrm{p}} \end{pmatrix} \tag{4}$$

can be deduced. In this work, focus is on

$$\underset{\sim}{F}^{\mathrm{p}} = \underset{\sim}{F}^{\mathrm{p}}_{\mathrm{dev}}\,\underset{\sim}{F}^{\mathrm{p}}_{\mathrm{vol}} = \begin{pmatrix} \lambda^{\mathrm{p}}_{\mathrm{devT}}\lambda^{\mathrm{p}}_{\mathrm{volT}} & 0 & 0 \\ 0 & \lambda^{\mathrm{p}}_{\mathrm{devT}}\lambda^{\mathrm{p}}_{\mathrm{volT}} & 0 \\ 0 & 0 & \lambda^{\mathrm{p}}_{\mathrm{devL}}\lambda^{\mathrm{p}}_{\mathrm{volL}} \end{pmatrix} \tag{5}$$

multiplicatively split into its deviatoric $\underset{\sim}{F}_{\mathrm{dev}}$ and volumetric $\underset{\sim}{F}_{\mathrm{vol}}$ parts, by considering that

$$\underset{\sim}{F}_{\mathrm{dev}} = J^{-1/3}\,\underset{\sim}{F} \tag{6}$$

where J is the Jacobian of the transformation, equal to $\det(\underset{\sim}{F})$, and prescribed to keep the unity value for an incompressible material. The true "plastic" strain tensor can be additively split as follows:

$$\underset{\sim}{\varepsilon}^{\mathrm{p}} = \begin{pmatrix} \varepsilon^{\mathrm{p}}_{\mathrm{devT}} + \varepsilon^{\mathrm{p}}_{\mathrm{volT}} & 0 & 0 \\ 0 & \varepsilon^{\mathrm{p}}_{\mathrm{devT}} + \varepsilon^{\mathrm{p}}_{\mathrm{volT}} & 0 \\ 0 & 0 & \varepsilon^{\mathrm{p}}_{\mathrm{devL}} + \varepsilon^{\mathrm{p}}_{\mathrm{volL}} \end{pmatrix}. \tag{7}$$

Unlike metallic materials, where the plastic strain is uniquely related to the deviatoric parts ($\varepsilon^{\mathrm{p}}_{\mathrm{devT}}, \varepsilon^{\mathrm{p}}_{\mathrm{devL}}$), the specificity here deals with an account for the "plastic dilation" (Ognedal et al. 2014) *i.e.* the volumetric plastic strains ($\varepsilon^{\mathrm{p}}_{\mathrm{volT}}, \varepsilon^{\mathrm{p}}_{\mathrm{volL}}$). Knowing the whole strain tensor in Equation (7), constitutive relationships allow the complete local stress tensor to be determined. The approach consists of introducing the symmetric left Cauchy Green strain tensor $\underset{\sim}{C} = \underset{\sim}{F}^{\top}\underset{\sim}{F}$ where the superscript $\top$ indicates transposition operation. In virtue of Equation (6), it follows that

$$\underset{\sim}{C}_{\mathrm{dev}} = J^{-2/3}\,\underset{\sim}{C}\,. \tag{8}$$

In addition, a deformation energy Ψ which is a particular case of the Helmholtz free energy is introduced, split also into isochoric (Ψ_{iso}) and volumetric (Ψ_{vol}) parts:

$$\Psi(\underset{\sim}{C}) = \Psi_{\mathrm{iso}}(\underset{\sim}{C}_{\mathrm{dev}}) + \Psi_{\mathrm{vol}}(J). \tag{9}$$

The second stress tensor of Piola-Kirchhoff $\underset{\sim}{S}$ can be derived from the deformation energy Ψ

$$\underset{\sim}{S} = 2\frac{\partial\Psi}{\partial\underset{\sim}{C}} = \underset{\sim}{S}_{\mathrm{vol}} + \underset{\sim}{S}_{\mathrm{iso}} \tag{10}$$

with

$$\underset{\sim}{S}_{\mathrm{vol}} = 2\frac{\partial\Psi_{\mathrm{vol}}(J)}{\partial\underset{\sim}{C}} = Jp\,\underset{\sim}{C}^{-1} = J^{1/3}p\,\underset{\sim}{C}^{-1}_{\mathrm{dev}} \tag{11}$$

where p is a Lagrange multiplier, and

$$\underset{\sim}{S}_{\mathrm{iso}} = 2\frac{\partial\Psi_{\mathrm{iso}}(\underset{\sim}{C}_{\mathrm{dev}})}{\partial\underset{\sim}{C}} = J^{-2/3}\,\underset{\approx}{P} : \left[2\frac{\partial\Psi_{\mathrm{iso}}(\underset{\sim}{C}_{\mathrm{dev}})}{\partial\underset{\sim}{C}_{\mathrm{dev}}}\right] \tag{12}$$

with $\underset{\approx}{P}$, a fourth order projection tensor into the deviatoric space, which can be expressed as

$$\underset{\approx}{P} = \underset{\approx}{I} - \frac{1}{3}\underset{\sim}{C}^{-1}\otimes\underset{\sim}{C} = \underset{\approx}{I} - \frac{1}{3}\underset{\sim}{C}^{-1}_{\mathrm{dev}}\otimes\underset{\sim}{C}_{\mathrm{dev}} \tag{13}$$

$\underset{\approx}{I}$ being the fourth order identity tensor and $\otimes$ operator defined as

$$(\underset{\sim}{A}\otimes\underset{\sim}{B})_{ijkl} = A_{ij}B_{kl}. \tag{14}$$

Once $\underset{\sim}{S}$ has been determined, the first Piola-Kirchhoff (engineering stress $\underset{\sim}{\Pi}$) and the Cauchy stress (true stress $\underset{\sim}{\sigma}$) tensors can be derived, following

$$\underset{\sim}{\Pi} = J\,\underset{\sim}{\sigma}\,\underset{\sim}{F}^{-\top} \tag{15}$$

$$\underset{\sim}{\sigma} = J^{-1}\,\underset{\sim}{F}\,\underset{\sim}{S}\,\underset{\sim}{F}^{\top}. \tag{16}$$

These first Piola-Kirchhoff and Cauchy stress tensors can also be split into their deviatoric and isostatic parts by applying the same operations as in Equations (15) and (16) to the stress tensor components in Equations (11) and (12), respectively. Furthermore, each stress tensor component is related to the corresponding deformation gradient. In particular, the volumetric component of the deformation gradient in Equation (5) or the strain tensor in Equation (7) are directly related to the isostatic stress tensor. This work aims at determining the complete deformation gradient tensor in Equation (3) and proposing a route to estimate, at the spherulitic scale, the local multiaxial Cauchy stress tensor in Equation (16), from 3D measurements.

3 Material, methods and data sets

3.1 Semi-crystalline isotactic polypropylene

The material under study is a semi-crystalline isotactic polypropylene (PP) with a glass transition temperature $T_g = -7.9\,^{\circ}\mathrm{C}$ and a crystallinity index $\chi = 47\,\%$, measured with the Modulated Differential Scanning Calorimetry (MDSC). Optical microscope examination on microtomed slices of the rectangular section is illustrated in Figure 2(a). This latter figure shows a through-thickness

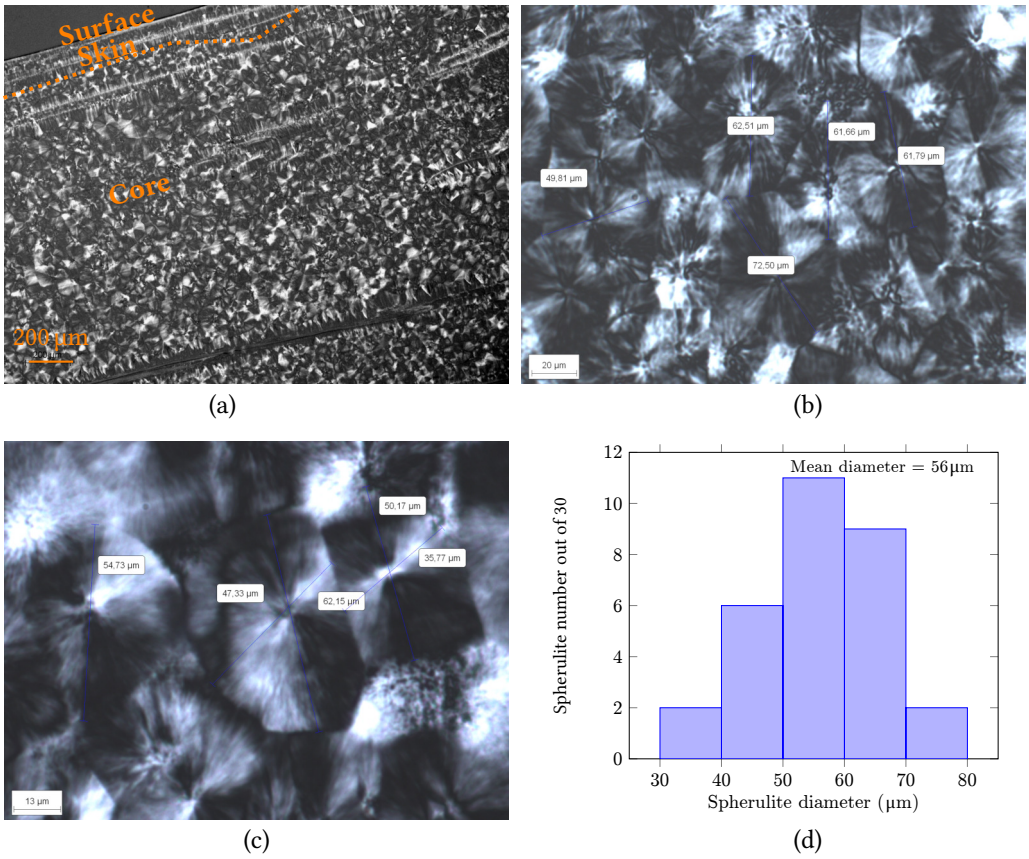

Figure 2 Optical microscopy examination of the spherulites on microtomed thin film of the PP under study: (a) Large surface; (b) and (c) Focuses on smaller surfaces to allow diameter measurements; (d) Histogram of the spherulite diameter measured on 30 net spherulites.

cut from a microtomed thin layer of the PP material at a large scale. The outer surface is indicated, and an orange dotted line has been drawn to approximately separate the skin part from the core. This skin-core effect, detailed in (Laiarinandrasana, Selles, et al. 2016), is due to the temperature gradient during the crystallisation process: the surface, in contact with the mould, experiences a higher cooling rate resulting in smaller spherulites. The transition from these small spherulites at the surface to the core is characterised by some oriented stripes, corresponding to trans-crystalline zones (Kantz et al. 1972; Assouline et al. 2001). Here, the skin is composed of both layers of small spherulites and the trans-crystalline zone; the end of this is characterised by the orange dotted line.

In the following, the presence of the skin zone has not been accounted for, but several examinations at this scale allowed the determination of an average thickness of the skin layer of about 350 µm from the outer free surfaces.

The present work focuses on the spherulites within the core. However, although spherulitic shapes could be distinguished in the core, from Figure 2(a), closer examination was required in some places, Figures 2(b) and 2(c), so as to allow measurements of the spherulite diameters. Actually, the field of view was optimised so as to let the boundaries of the spherulite to be well resolved in the micrograph.

From about 30 spherulites with clear morphology, the histogram of the measured diameters was plotted in Figure 2(d). They were observed to be rather equiaxial, with an average diameter of about 56 µm. This isotropy in the morphology and this initial value of the diameter are of crucial importance for the determination of the spherulitic strains when the specimen is stretched. Note that the minimum and maximum measured diameters were respectively 30 and 80 µm.

In (Laiarinandrasana, Selles, et al. 2016), dog bone ISO flat specimens of PP, with a gauge length of 25 mm were used. They were tested at 20 °C and at a relative humidity of 50 % thanks to an electromechanical tensile rig at various strain rates. The samples tested at a strain rate of $4 \times 10^{-4}\,\mathrm{s}^{-1}$ were selected to be analysed here. Recall that the tensile test ran until the plateau stress, after having experienced the peak stress and stress softening. The tests were stopped once the deformed sample exhibited an extended necked region, allowing two samples to be inspected at the European Synchrotron Radiation Facility in Grenoble (France). The first one was examined by using the tomography technique, for which some results at a resolution corresponding to 1 px $\approx$ 0.7 µm were reported in (Laiarinandrasana, Selles, et al. 2016). To go further, the present study addresses the second sample using the holotomography technique, as detailed in (Morgeneyer et al. 2014; Ovalle et al. 2021), which allowed a better resolution, as high as 1 px $\approx$ 50 nm.

3.2 Volumes of interest *versus* representative volume elements

The representative volume element (RVE) definition implies a homogeneous (or homogenised) medium where the stress and the strain are homogeneous as well. At the macroscopic scale, two RVE were introduced, noted respectively as "skin" and "core". The skin RVE was supposed to correspond to the gauge length of the specimen (25 mm × 4 mm × 2 mm). Note this skin RVE assumed a homogenised volume where the skin-core effects were ignored. By subtracting the skin thickness (about 0.7 mm), the core RVE was reduced to (25 mm × 3.3 mm × 1.3 mm). The core RVE was supposed to be composed of an ensemble of spherulites regardless of the distribution of their sizes.

As soon as necking appeared, at the peak stress, these RVE contained a strain localisation around the neck. In this region the stresses and strains were expected to exhibit a gradient and a triaxiality ratio. Here, the interest was to study the measured displacements/strains at three scales. Three volumes of interest (VOI) are considered, similar to those illustrated in (Laiarinandrasana, Selles, et al. 2016). As mentioned above, these VOIs were examined by the Synchrotron Radiation Tomography/Holotomography technique at two resolutions for which 1 px corresponded, respectively, to 0.7 µm (Laiarinandrasana, Klinkova, et al. 2016) and 50 nm (Morgeneyer et al. 2014). Accordingly, three scales of VOI were analysed: macroscopic at the surface (skin), at the level of the core and at the scale of the spherulite.

3.3 Data sets and metrology

As mentioned above, the present study attempts to analyse in detail a necked region. To this end, Figure 3 recalls the three VOIs corresponding to tomographic data sets at a resolution of 0.7 µm. At the bottom of the figure, the selected cylindrical coordinates have been sketched, z, r and θ were associated with respectively the longitudinal, width and thickness directions. Note that r and θ directions may be called the transverse direction meaning, respectively, through diametrical, width and thickness for spherulite and core/skin volumes. The scale is given at the bottom of Figure 3.

For the sake of clarity, it should be noted that:

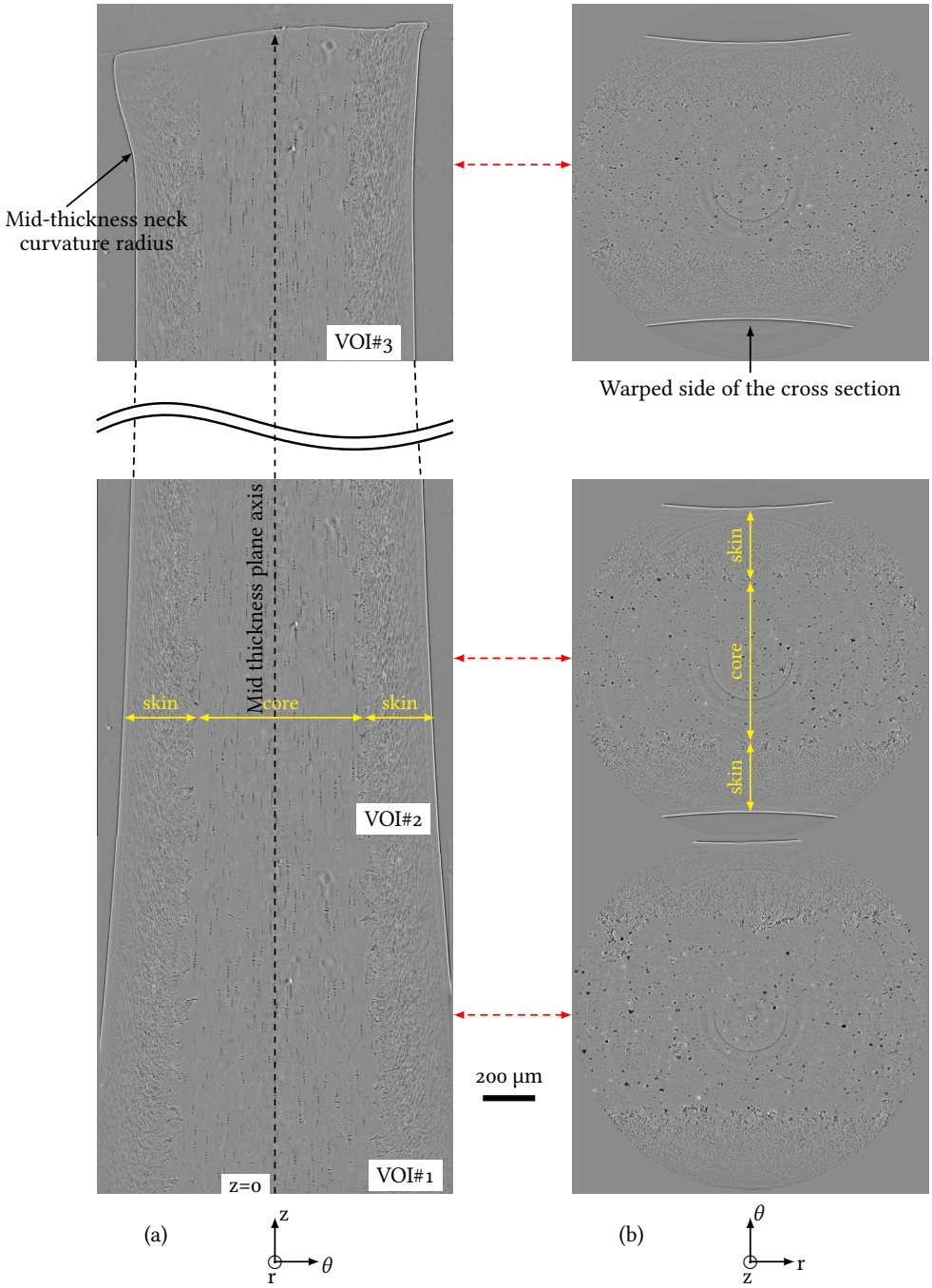

Figure 3 Three microtomography data sets representative of the Volumes of interest (VOI): (a) Side views at mid-width cuts; (b) Corresponding top views of respective VOIs. *Yellow arrows indicate the core/skin regions allowing their thicknesses to be measured.*

- Figures 3(a) and 3(b) correspond respectively to side and top views of the three VOIs where VOI#3 (at the top) was the more necked region;
- the side views in Figure 3(a) correspond to mid-width virtual cut of the tomographic data set in 3D instead of the commonly used mid-thickness cut to see the neck through the width. Actually, the width was too large compared with the field of view of the synchrotron radiation tomography setup;
- experimental artifacts did not allow consecutive data sets to be obtained, a VOI located between VOI#2 and VOI#3 is missing due to a failure of the reconstruction. In the data sets, cavities are in black, polymer matrix is in grey and intervoid walls, and inclusions, are in brighter grey, or even in white.

In Figure 3(b), warping of the side was systematically observed especially on VOI#3 as commented in the figure. Therefore, the observation at mid-width corresponded to the minimum

thickness when the sample was deformed. Additionally, in each picture, the skin and the core can be distinguished. As a matter of fact, the skin is more warped than the core, the cross-section of which remained more rectangular.

From Figure 3, characteristic lengths were deduced. To this end, Figure 4 plots the relative position of the VOIs associated to the measured thicknesses. It should be mentioned that:

- the origin of the coordinate $z = 0$ is the bottom line of VOI#1;
- the total height of the studied deformed sample was 5.7 mm;
- The keys indicating VOI numbers were positioned at the barycentre of each VOI. Each measurement on the VOI is displayed at the coordinate of its barycentre.

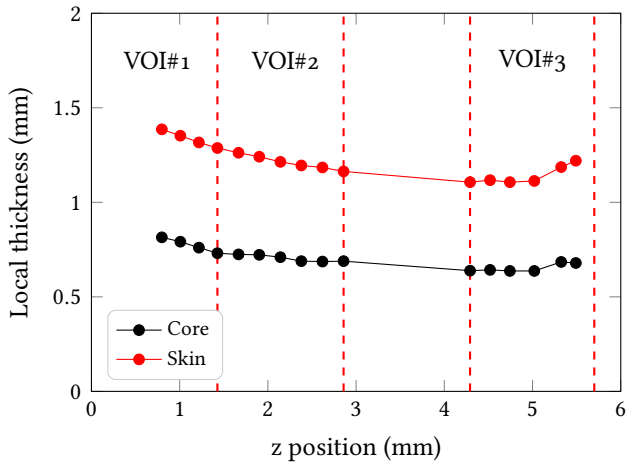

Figure 4 Profiles of the core and skin according to z. Relative position and characteristic heights of the VOIs.

It can be observed that the thickness is not constant for each VOI, neither for the surface (skin) nor for the core of the sample. Nevertheless, the initial through thickness gauge length was the same; that is 1.3 mm and 2 mm, respectively, for the core and the "skin" of the macroscopic sample.

At the microscopic scale, the deformed spherulites are used as markers for the measurements of the deformation. After a comprehensive study of 3D images, it turned out that, in Figure 3(b), the boundary of the spherulites was more discernible than in Figure 3(a). A systematic study of the 3D-shapes of deformed spherulites was then performed so as to obtain the longitudinal extension and the lateral contraction/dilation at two resolutions obtained by Synchrotron Radiation Computed Tomography.

4 Results

4.1 Analysis of the characteristic morphology of deformed spherulite

Figure 5 displays various views in 3D of deformed spherulites at a resolution corresponding to 1 px = 0.7 µm. An attempt was made to isolate one deformed spherulite in the centre of a cube with 140 µm sides, see Figure 5(a). This side view corresponds to a longitudinal cut of this cube through a plane containing the central part including the nucleus of the spherulite. The nucleus and polar fans (Pawlak et al. 2008) composed of materials (in bright) and penny shaped voids (black) piled up in columns can be clearly seen. This specific structure of double polar fans is generally accepted to be included inside a spherulite. For the PP under study, the boundary of the spherulite could be identified, illustrated by the path composed of yellow dotted lines drawn in Figure 5(a). However, whilst the polar fans are clearly shown, the boundary of the spherulite could not be retrieved as an ideal ellipse but showed a polygonal shape. In the top face of Figure 5(a), circular voids are discernible. This top face shows, as sketched in Figure 1(b) (top view), a central circular void surrounded by the boundary of the spherulite (yellow dotted line), which is not circular but polygonal. Additionally, as indicated in Figure 5(a) a pile up of several equatorial voids along the tensile direction (on about 2/3 of the height of the spherulite) was observed. Their shape is rather tortuous and cannot be represented as a simple plane. They show

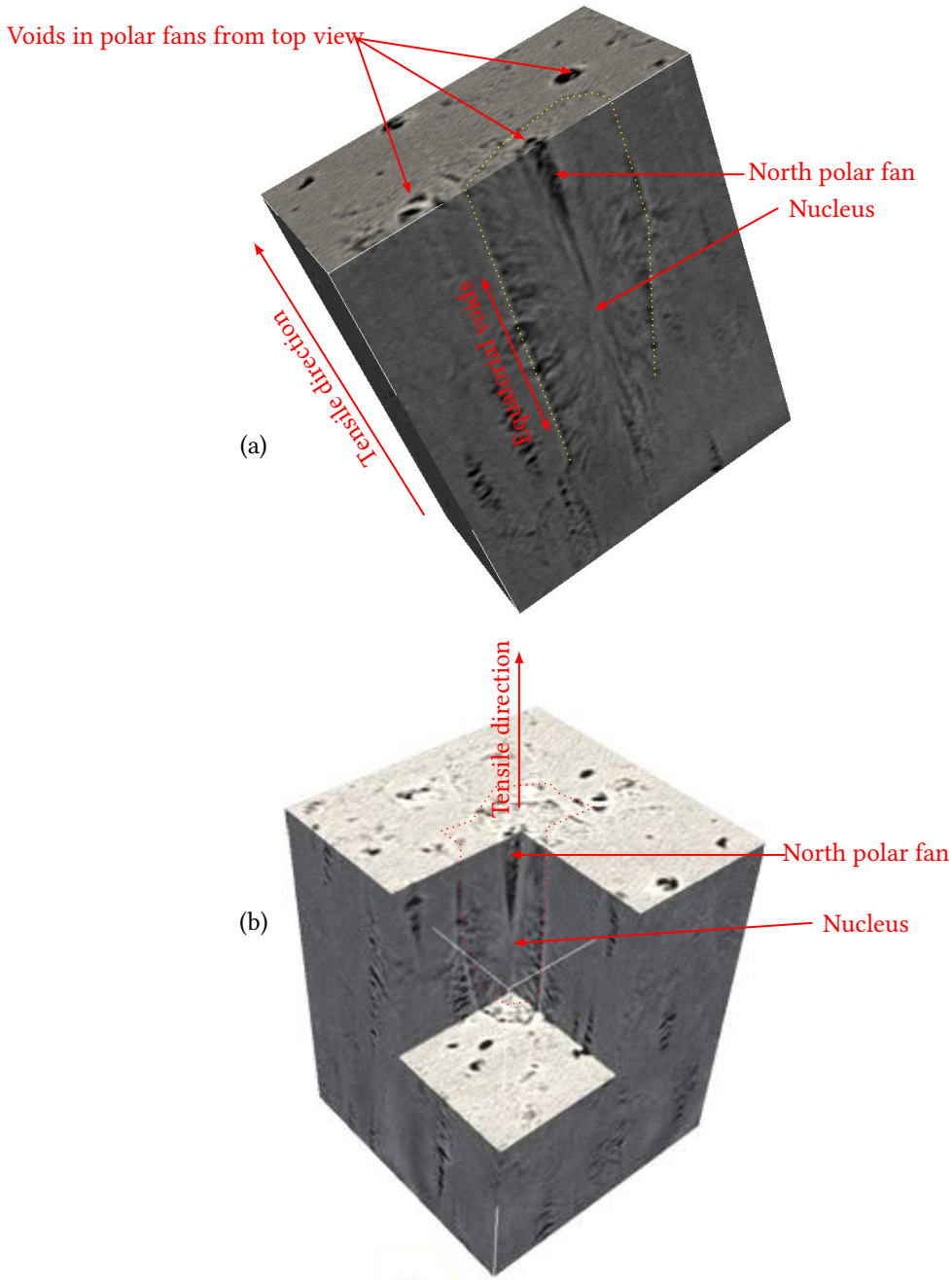

Figure 5 Various 3D views of deformed spherulites showing polar fans, from data sets obtained from Synchrotron Radiation Tomography with a resolution corresponding to 1 px ≈ 0.7µm. *Cube side about* 140 µm.

also a general inclination angle depending on their location: 0° *i.e.* perpendicular to the tensile direction at the equatorial zone; and less than 45° when located away from the equator.

To go further in the 3D description, Figure 5(b) shows the cube in perspective where a transparent box of approximately 1/8 of the cube was inserted, so as to display the microstructure inside the spherulite. The "North" polar fan of the spherulite is visible through the vertical line crossing the centre of the cube. The polygonal boundary of the spherulite (red dotted lines) around the north polar fan is clearly visible. The bottom face of the transparent box cuts the south part of the spherulite partially revealing the "South" polar fan. In addition, the top view reveals more or less dashed lines corresponding to the boundary of the spherulite. Actually, the diameter of a spherulite is easier to determine from the top view than from the side view.

Several attempts were made, by using Avizo software, to operate a surface rendering of the spherulite boundaries together with the polar fans, but the images were not satisfactory. In fact, the spherulites were so nested in the side view that it was difficult to obtain fair quantification of the characteristic distances (diameters and heights). A better resolution applied on a few

spherulites allowed the details of these patterns to be identified. The nano-tomography (or holotomography) technique as used by Morgeneyer et al. (2014); Ovalle et al. (2021) was used here, the resolution corresponded to 1 px = 50 nm.

The tomographic data set with a resolution corresponding to 1 px = 50 nm was selected in the centre of a necked region. This was composed of a cylindrical volume of 102.4 µm in both diameter and height.

Figure 6 corresponds to the side views (longitudinal cut) of the nano-tomographic data set. As indicated by the black arrow, the tensile direction is vertical. The polar fans already reported for various semi-crystalline polymers (Pawlak et al. 2008; Pawlak et al. 2010; Rozanski et al. 2013) were the basic pattern from which the image recognition is based in the following. In Figure 6(a), a couple of polar fans are highlighted with vertical dashed red arrows indicating their boundaries. Focusing first on the detail of the polar fans (right border of Figure 6(a)), four columns of penny-shaped voids (in black) separated by matter (in light grey) can be observed. Their diameter increases when voids are located away from the centre. Inside the voids some transverse fibrils could also be observed, and the void morphology was rather "curved" like spherical caps. Moreover, the cylindrical nucleus described by Selles et al. (2017); Raphael et al. (2019) is clearly revealed in-between the north and the south polar fans.

Focusing on the second polar fans surrounded by the four vertical dashed red arrows located in the middle of Figure 6(a), three voids nucleated from nanometric particles (in white inside the black void) are indicated by horizontal red arrows. In particular, the void named as P#1 is located in the centre of the nucleus. These voids emanating from nano defects (P#1, P#2 and P#3) are much smaller than those inside the polar fans. It can therefore be concluded that critical voids are due to the spherulitic microstructure and not from nanoscopic defects in the material.

From this side view and even at this resolution, again the boundaries of spherulites are not well resolved. Although the vertical red dashed arrows seem to indicate that they are straight, it is easier to determine the total height of the polar fans (north and south) and attribute this to that of the deformed spherulite.

Figure 6(b) displays the whole side view (longitudinal cut) of the nano-tomographic data set where three entire polar fans are visible together with four partial polar fans. Three spherulites named as Sph#1, Sph#2, Sph#3, were considered here.

- Sph #1: located in the top left of Figure 6(b). The nucleus is illustrated by a vertical red dashed rectangle. It was noticed that this nucleus contained more than seven voids (in black) having nucleated from particles (in bright inside each void). The nucleus has therefore been extended much more than the others observed in the same data set;
- Sph #2: a nucleated void, surrounded by a red square, was noticed as well in the central region of the nucleus. Additionally, the south end of the polar fan is hidden probably by the forefront; meaning the polar fan may be slightly tilted. A vertical cut cannot show the whole polar fans inducing uncertainties on the measurement of the height of the spherulite;
- Sph #3: the south polar fan is clearly seen with discernible boundaries: the lateral boundary is indicated by the vertical dashed red arrow (top right) whereas the inter-spherulitic region ending the spherulite is located in-between the inclined red dashed arrows.

Figure 7 focuses on 2D cuts indicating the top views, the tensile direction being normal to these images. Figure 7(a) illustrates the global view at this scale. The essential pattern consisted of a void (in black) surrounded by a polygon, with sometimes stripes linking the central void to the sides of the polygon. Depending on the size of the central void, the stripes assumed to be the crystalline and amorphous lamellae could be distinguished: the smaller the voids, the more discernible the lamellae. Recall that smaller voids were located close to the nucleus for the polar fans microstructures.

Figure 7(b) illustrates a magnification of the images on a few spherulites. The difference in grey level for adjacent spherulites allowed a better identification of their boundaries, drawn in red dotted lines. The details of each of the four labelled spherulites (Sph) can be summarised as follows:

- Sph #1: the centre is in light grey without any void meaning that the horizontal cut is through the nucleus which is denser. The lamellae linking the nucleus and the polygonal boundary of this spherulite are visible;

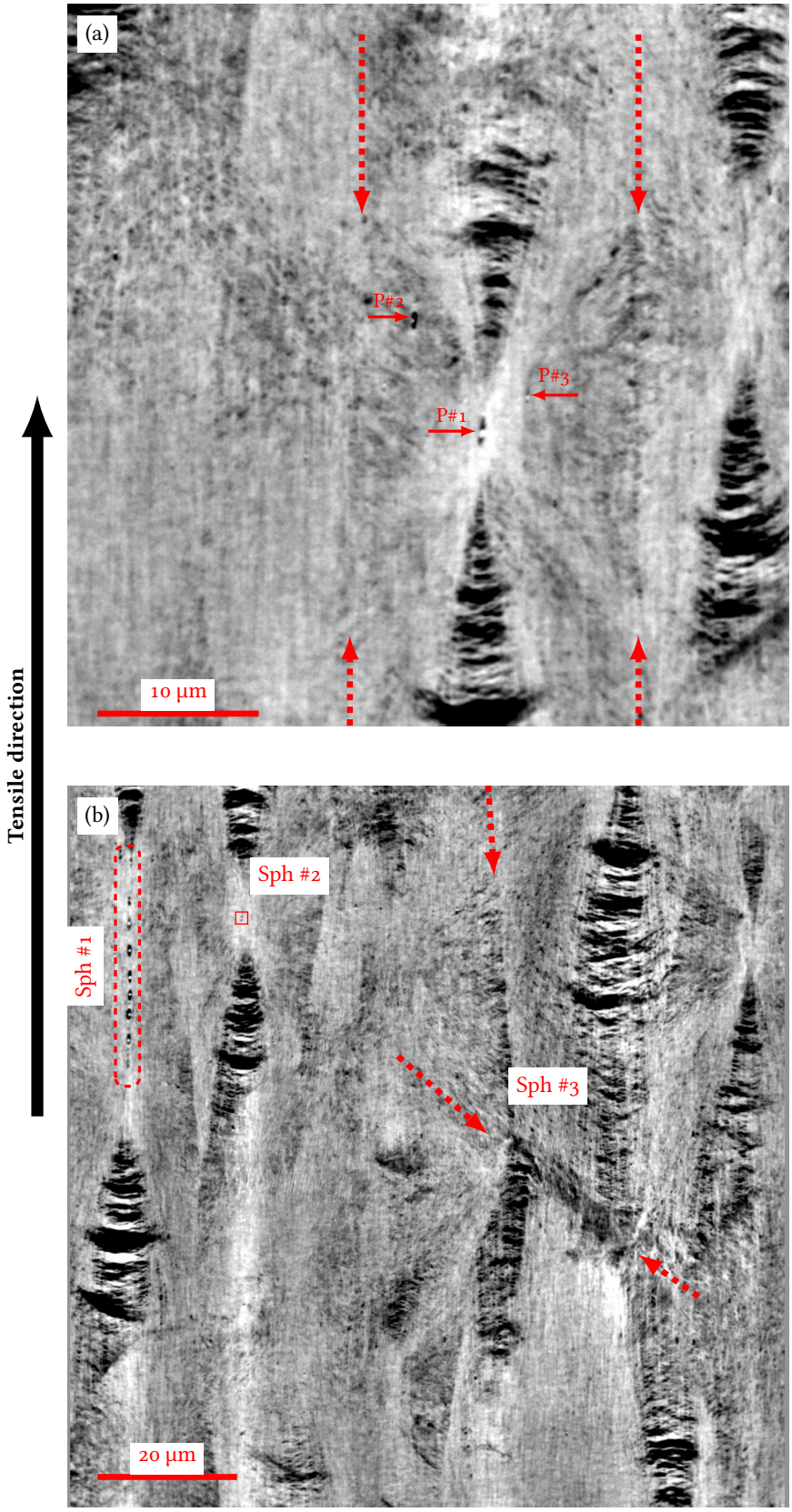

Figure 6 Side views of the data set of deformed PP at a resolution of 50 nm: (a) detailed view of a couple of polar fans; (b) global view 102 µm × 102 µm.

- Sph #2: the centre is also in the dense nucleus, the stripes are visible from the nucleus to the boundaries. In the bottom left boundary of this spherulite (8 o'clock), a void can be observed. At this location, it is probably either an equatorial void or an inter-spherulitic void (or together both);
- Sph #3: the centre is composed of a small void that is at the beginning of a polar fan, so rather

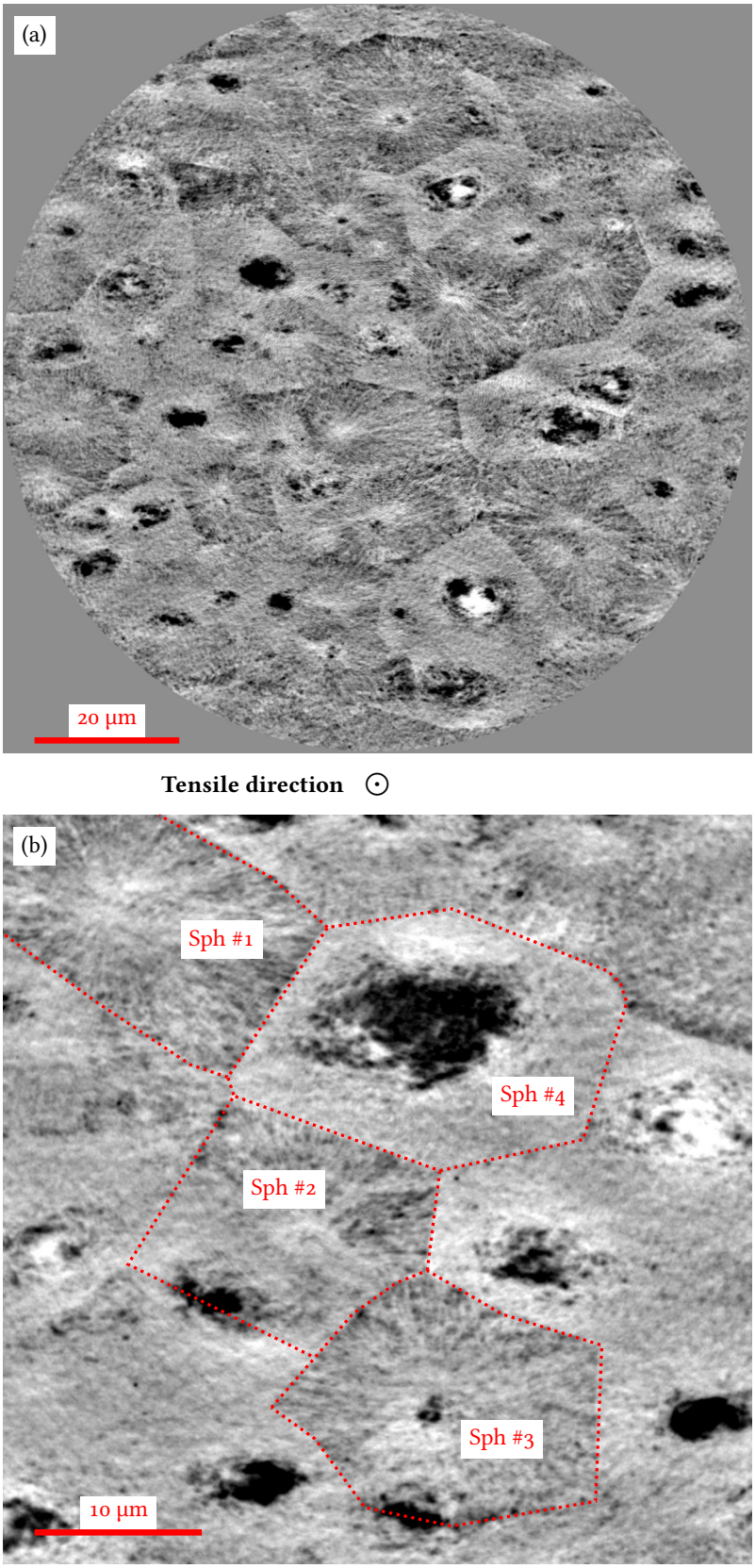

Figure 7 Top views of data set of deformed PP at a resolution of 50 nm: (a) global view 102 µm × 102 µm; (b) closer look at few spherulites: 45 µm × 45 µm.

closer to a nucleus basis. The lamellae and an inter-spherulitic void (7 o'clock) are also visible ;

- Sph #4: the centre is composed of a large cluster of voids. The lamellae cannot be distinguished. Clearly, the horizontal cut was done at the end of a polar fan (close to the inter-spherulitic matter).

Given the above-mentioned resolution of the polygons of spherulites' boundaries, the top views will be used for the measurement of the diameters of the deformed spherulites. By recognising the pattern in the top view, about 40 and 10 spherulites were identified in Figures 7(a) and 7(b), respectively.

4.2 Analysis of spherulites inside the VOIs

So as to obtain the maximum number of spherulites and taking advantage of the patterns recognised from the nano-tomography, the analyses were carried out on the three data sets with the resolution corresponding to 1 px = 0.7 µm.

Figure 8 focuses on 2D cuts showing the top views of the three VOIs. The cylindrical coordinates are recalled in the bottom of the figure. Whereas Figure 8(a) displays the reconstructed

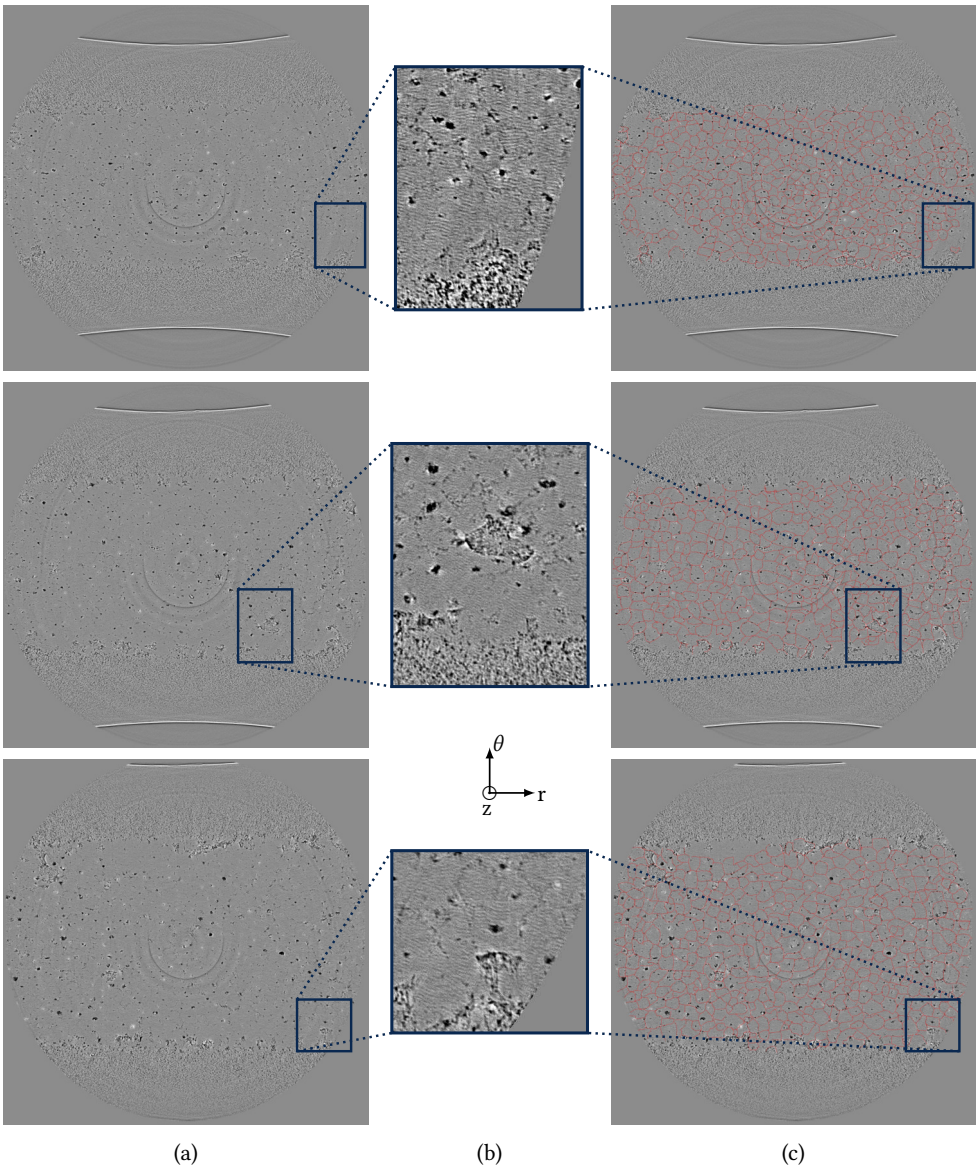

Figure 8 2D section top views of microtomography data of the three VOIs presented in Figure 3 so as to determine the diameters of the deformed spherulites: (a) Reconstructed images; (b) Closer examinations of a specific region; (c) Drawings of the identified boundaries for the deformed spherulites.

tomographic images of the three VOIs, in Figure 8(b), closer examination at precise regions delimited by the dark blue rectangles are illustrated. It aims at identifying the polygonal boundaries of the spherulites. The required magnification depended on the grey level of the zone in Figure 8(a), so that the three images in Figure 8(b) are not at the same scale. It should be noted that even though not well resolved, the spherulites boundaries could be identified on images as in Figure 8(b). These boundaries were then drawn in red in Figure 8(c). By pairing the

data sets in Figure 8(a) by rectangles with approximately the same magnification factor as in Figure 8(b), the identified spherulites boundaries have been drawn in the whole initial image. For comparison purposes, the same region has been illustrated by the small corresponding rectangles in Figure 8(a) and Figure 8(c). The red lines allowed the digitisation of Figure 8(c), from which statistics on the spherulites diameters could be performed.

More than 300 recognised polygonal boundaries of deformed spherulites were manually identified as such. It can be noticed that only spherulites in the core could be treated. For each identified spherulite, two perpendicular diameters were measured, respectively along r and θ directions.

Using the same approach as in Figure 8, Figure 9 focuses on the side views of the three VOIs. This time, Figure 9(a), showing again the reconstructed tomographic images, has already

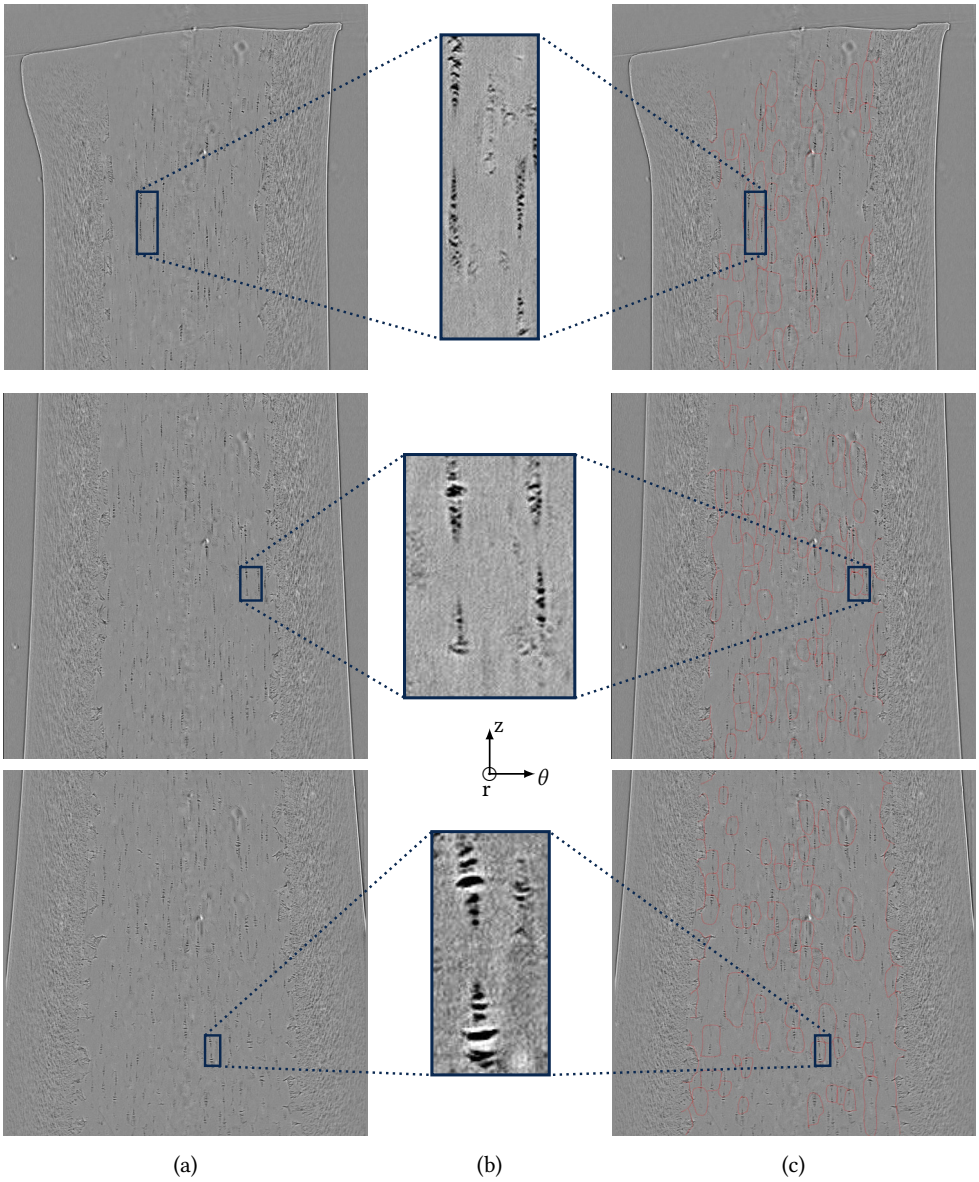

Figure 9 Side views of the three VOIs presented in Figure 3 so as to determine the heights of the deformed spherulites: (a) Reconstructed images; (b) Closer examinations of a specific region; (c) Drawings of the identified polar fans inside the deformed spherulites.

been used for the determination of the heights of the deformed spherulites, by referring to the polar fans in (Laiarinandrasana, Klinkova, et al. 2016). Figure 9(b) shows again specific zones, magnified, so as to allow the recognition of the polar fans. Drawings of the boundaries of the deformed spherulites in each VOI are given in Figure 9(c). Only the spherulites in the core were taken into consideration. Due to the high interlacing of the deformed spherulites from these views, an average of 50 deformed spherulites were utilised for the height measurements, along

the z direction in the cylindrical coordinates.

4.3 Histograms of characteristic lengths of deformed spherulites

Figure 10 focuses on the diameters measured on the deformed spherulites in the three VOIs. The numbers of the identified spherulites explored are displayed in the ordinates of the histograms. The columns (a) and (b) correspond to the r and θ-diameters respectively. The mean value of

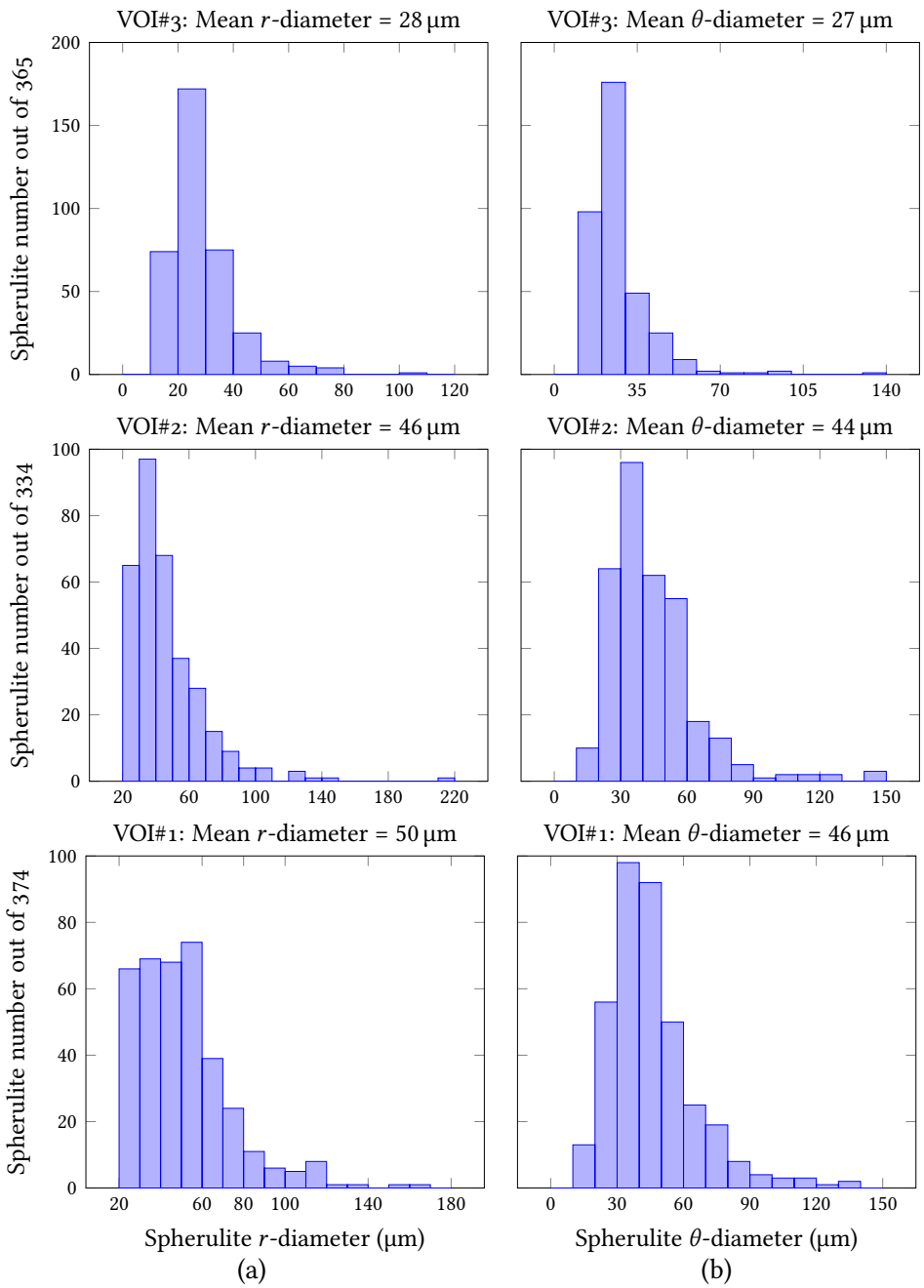

Figure 10 Histograms of the diameters of the identified deformed spherulites in the core, for VOIs#1,2,3 from bottom to top: (a) diameter along r-direction; (b) diameter along θ-direction (See Figure 8 for the cylindrical coordinates).

the diameter together with the number of the prescribed VOI have been indicated within each histogram. For each VOI, r and θ-diameters were observed to be similar: the deformed spherulites exhibited, at least, transverse isotropy. Moreover, the closer to the maximum necked region (minimum thickness), the lower the value of the spherulite diameter. Note also that although the histograms are not at the same scale, the mean diameters are shared by less and less deformed spherulites in respectively VOI#1, VOI#2 and VOI#3. In other words, the histograms are "more flat" in VOI#1 than in VOI#3; or the statistical mode value is more distinct in VOI#3 than in VOI#1.

The same analysis was performed on the height of the deformed spherulites in Figure 11, focusing on the side views. This time, only one histogram was plotted for each VOI based on the

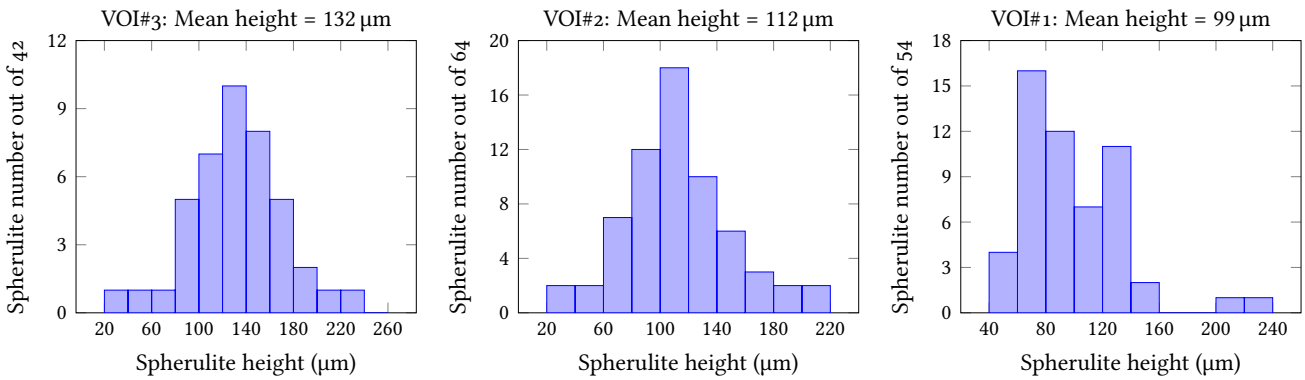

Figure 11 Histograms of the heights of the identified polar fans in the core along the z direction.

height of the polar fans (z direction) as mentioned above. Again, the histogram is "more flat" in VOI#1 than in VOI#3. The mean values of the height continuously increase from VOI#1 to VOI#3.

4.4 Elongations measurements

Once the average values of the spherulite diameter, the thickness and the height corresponding to each VOI were obtained, this subsection attempts to determine the elongations for each VOI. Three scales were then considered, consisting of: the spherulitic, the core and the macroscopic (named as skin). For the two first scales, each VOI was assumed to be the RVE where the calculated elongation was supposed to be homogeneous. The values determined for each VOI will be assigned to its barycentre.

Gauge lengths at three scales The elongation λ is defined as L/L_0 where L_0 is the gauge length of the RVE. Table 1 summarises this gauge length for each VOI. These values will be used in the following. The material is assumed to be isotropic, only two elongations were considered:

	Spherulite		Core		Skin	
Lengths (µm)	Avg. diameter	Avg. height	Min. thickness	VOI height	Min. thickness	VOI height
VOI #1-2	56	56	1300	784	2000	784
VOI #3	56	56	1300	672	2000	672

Table 1 Estimated or measured gauge lengths.

a longitudinal one corresponding to the height and a transverse one attributed to the spherulite diameter and the minimum (at mid-width) thickness for the core and the skin VOI.

It should be mentioned that:

- For the spherulites: due to a good initial circularity (sphericity), for the three VOIs, the two directions have similar gauge lengths, equal to the average spherulite diameter (56 µm);
- For the core VOIs: as mentioned in Section 2.1, the initial thickness was equal to 1300 µm. Concerning the initial height, the number of deformed spherulites in Figure 9(b) along a vertical line was determined for each VOI. The result was 14 and 12 for respectively VOI#1-2 and VOI#3. The "average" initial height was obtained by multiplying the latter numbers by 56 µm;
- For the skin VOIs: as mentioned in Section 2.1, the initial thickness was equal to 2000 µm. The same initial height as for core VOIs was selected.

Measured characteristic lengths Table 2 displays the measurement of various specific lengths from deformed VOIs. Due to large deformation measured, the elongation, defined as the ratio of the deformed length, related to the initial length, was selected for each VOI. As mentioned above, irreversible deformations were measured. For the sake of simplicity, the subscript p (for plastic or irreversible phenomenon) will not appear in the following on the elongation.

	Spherulite		Core		Skin	
Lengths (µm)	Avg. diameter	Avg. height	Min. thickness	VOI height	Min. thickness	VOI height
VOI #1	48	99	814.8	1430	1386	1430
VOI #2	45	112	709.8	1430	1214	1430
VOI #3	27.5	132	637	1331	1110	1331

Table 2 Characteristic lengths measured on deformed VOI.

From Tables 1 and 2, the longitudinal $\lambda_L \geqslant 1$ and transverse $\lambda_T \leqslant 1$ were introduced so as to plot their evolution along the z-position of the three VOIs in Figures 12 and 13, respectively. The deformation of the skin obtained at the surface was the same as that measured by classical

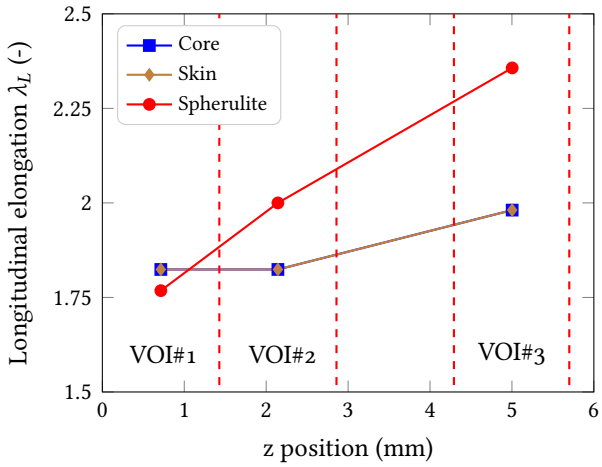

Figure 12 Evolution of the longitudinal elongations (λ_L) along the necked region.

experimental techniques such as extensometer or digital image correlation. Then, the assumption commonly used is the homogeneity of the deformation through the thickness. Checking this homogeneity is one of the novelties of the present work.

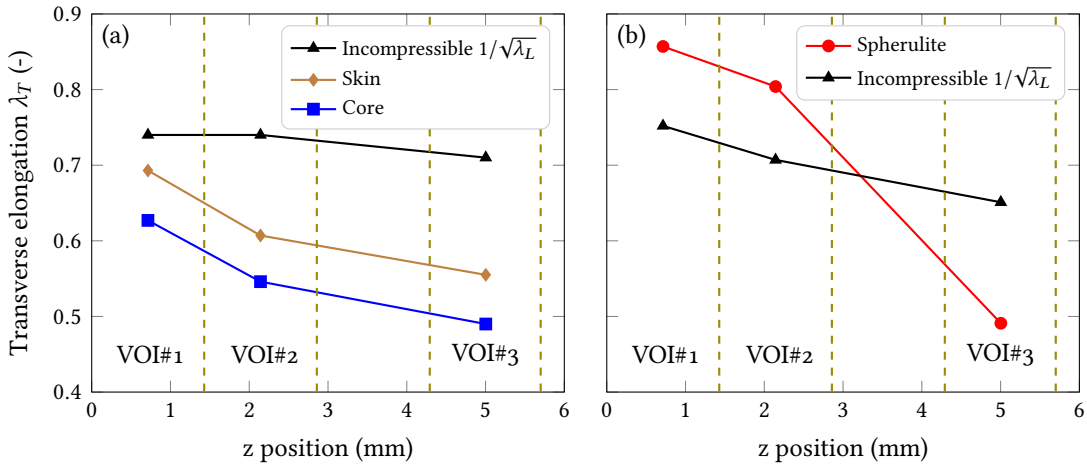

Figure 13 Evolution of the transverse elongations (λ_T) along the necked region: (a) Core and skin; (b) at the spherulitic scale.

Evolution of the longitudinal elongations Figure 12 shows the evolution of the longitudinal elongation λ_L from the bottom of the neck (less necked region = VOI#1) to the most pronounced necked region VOI#3.

By construction, the longitudinal displacements of both skin and core were similar, giving the same spatial evolution of λ_L (open brown diamond and blue square symbols). The equality

between the skin and core λ_L obtained here means that 3D imaging technique could not detect slipping at the skin–core interface, which was not well resolved.

A continuous increase of this longitudinal elongation is observed: sligthly from VOI#1 to VOI#2 but more significantly from VOI#2 to VOI#3. The linear increase, with a steeper slope, in deformation of the surrounding region was clear at the spherulitic level. Note that, for VOI#1, λ_L was approximately the same for the three scales of analysis. At this location -near the non-necked zone- the deformation can be considered as homogeneous through the thickness. Conversely, for VOI#2 and #3, λ_L in the central part (mid-thickness) was higher than those of the core and the skin. The more critical the necking (VOI#3), the bigger the difference between the λ_L at the surface and in the centre.

The ratio between the macroscopic elongation at the surface and that at the scale of the spherulite started at 1 (in VOI#1) then increased to 1.1 (in VOI#2) and reached 1.2 (in VOI#3). It can be concluded that a heterogeneity in elongation was highlighted in the necked zone. The gradient of λ_L was the highest where the necking was the most critical along the necked zone. The amplification of the elongations was estimated to be in the range of [1, 1.2]. In terms of logarithmic true strain, the magnification went from 1 to 1.15 and ending up to 1.25.

Evolution of the transverse elongations The following discussion holds for tensile tests *i.e.* $\lambda_L \geqslant 1$. The corresponding transverse elongation λ_T allows the analysis of the so-called Poisson's effect at the three scales of observation. In terms of elongation $\lambda_T \leqslant 1$ for negative deformation during longitudinal tensile loading. For isotropic materials, the value of λ_T allows the comparison with the Poisson's ratio ν in small deformation. Indeed, the true logarithmic strain being defined as $\ln(\lambda)$,

$$\nu = -\frac{\ln(\lambda_T)}{\ln(\lambda_L)} \tag{17}$$

Accordingly,

- the incompressibility constraint set by $\nu \simeq 0.5$ corresponds to $\lambda_T \simeq 1/\sqrt{\lambda_L}$;
- if $1/\sqrt{\lambda_L} \leqslant \lambda_T$, then $\nu \leqslant 0.5$;
- else if $1/\sqrt{\lambda_L} > \lambda_T$, then $\nu > 0.5$.

With these considerations, Figure 13 plots the transverse elongations together with the line corresponding to $1/\sqrt{\lambda_L}$ for the sake of comparison.

Figure 13(a) analyses λ_T data at the mesoscopic scale (skin and core). By opposition to λ_L, see Figure 12, the measurements at the skin (surface) differed from that at the core, obtained by 3D-imaging. Both λ_T were below $1/\sqrt{\lambda_L}$ curve for all VOIs all along the necked region. At the surface and at the interface between skin and core regions, $\nu \geqslant 0.5$.

The average transverse elongation of spherulites is plotted in Figure 13(b) and compared with $1/\sqrt{\lambda_L}$ curve (black triangle and solid line). In contrast with the aforementioned results at the macroscopic scale, here, both VOI#1 and VOI#2 exhibited $\lambda_T \geqslant 1/\sqrt{\lambda_L}$. Only VOI#3 showed an accordance with the observation at macroscopic scale, *i.e.* $1/\sqrt{\lambda_L} \geqslant \lambda_T$.

These key results are of prime importance in allowing a discussion about the difference of volume change between the macroscopic (at the surface) and the spherulitic scales.

Evolution of the volume change For large strain formulation, the volume change is given by the Jacobian of the transformation J. By assuming isotropy of the material, the elongations through the width and the thickness are supposed to be equal to λ_T. Therefore, J theoretically gives:

$$J = \frac{V}{V_0} = \lambda_L \times \lambda_T^2 \tag{18}$$

In virtue of Equation (17), J is equal to unity in the case of zero volume change ($\nu = 0.5$) which is commonly denoted as an incompressibility constraint of the material.

$J \geqslant 1$ or equivalently $\lambda_T \geqslant 1/\sqrt{\lambda_L}$ or $\nu \leqslant 0.5$ means a volume increase, due to a significant longitudinal extension without "sufficient" lateral contraction. By contrast, $J \leqslant 1$ ($\lambda_T \leqslant 1/\sqrt{\lambda_L}$ or $\nu \geqslant 0.5$) corresponds to a volume loss due to too large contraction in comparison with the lateral extension. These comments are valid under tensile loading in the longitudinal direction. In the

case of compressive loading in the same longitudinal direction, there is a volume decrease ($J \leqslant 1$) and the volume increase ($J \geqslant 1$) corresponding to $\nu \leq 0.5$ and $\nu \geq 0.5$, respectively.

The above-mentioned volume decrease under tensile loading, denoted also as "compaction" or "densification" of the material, began to be reported in the literature when Digital Image Correlation (DIC) became of common usage (Gaucher-Miri et al. 1997; Cangemi et al. 2004; Addiego et al. 2006; Ponçot et al. 2013).

At the microscopic scale, Xiong et al. (2018) reported the same phenomena (volume increase or loss) depending on the location considered in the spherulite, that is in the equatorial or polar regions.

Figure 14 illustrates the calculated volume change, using Equation (18), along the longitudinal path on the necked region. The horizontal line at $J = 1$ symbolises the incompressibility constraint, *i.e.* no volume change.

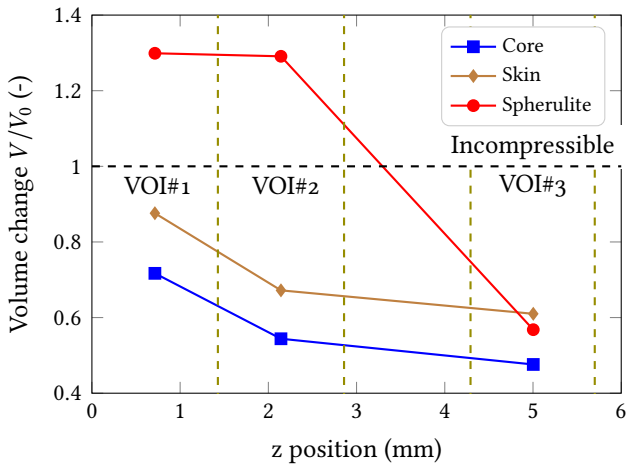

Figure 14 Evolution of the volume change V/V_0 along the necked region.

It can be observed that both skin and core exhibited a volume decrease along the necked region from VOI#1 to VOI#3. By contrast, the volume related to the spherulites was observed to increase, except for VOI#3. These observations highlighted a strong heterogeneity in the volume change through the thickness, depending on the degree of necking. The measurement at the surface showed an apparent compaction all along the necked region. Traditionally, the determination of the volumetric deformation has been carried out by integrating the volume change using the measurement at the surface and assuming its homogeneity through the thickness. These above-mentioned observations showed that this approach is highly questionable.

Focusing on the measurement at the spherulitic scale (full red circle in Figure 14), a volume increase (positive volumetric deformation) could be measured on VOI#1 and VOI#2. Whereas the amount of this volume increase diminished from VOI#1 to VOI#2, it completely switched into a volume loss (negative volumetric deformation) in VOI#3.

In the next section, a discussion about the micro-mechanisms inducing the nature of volume change is proposed. Additionally, the consequences of these results on the so-called "intrinsic" stress-strain curves are highlighted.

5 Discussion

5.1 Micro-mechanisms of deformation and voiding inducing volume change

In the following, the above-mentioned mechanisms of void evolution, in the three VOIs will be assumed to follow the same trend as for increasing deformation. This means that the "average spherulite" in VOI#1 and VOI#2 will be supposed to experience the same void growth mechanisms as those occurring during the stress softening (appearance and gradual extension of the necking at the surface). VOI#3 corresponds to the plateau where the necked matter, far from the shoulders is stabilised in lateral displacement, whilst the neck is still extending longitudinally.

At the spherulitic scale, the volume increase in VOI#1 and VOI#2 is then ascribed to the void appearance and growth in the beginning of the necking. Although the void nucleation depends on the resolution of the technique, Selles et al. (2017) reported for Polyamide 6 that the first appearance of voids under nano-tomography corresponded to the peak stress. At this very beginning of the stress softening, the amount of voids induces a volume increase due to:

- a longitudinal "over-extension" caused by the height of these cavities, added to the local extension of matter left in-between the penny shaped voids. The longitudinal elongation λ_L combines these two contributions;
- a lateral expansion due to void appearance compensated by the contraction caused by both Poisson's effect and shrinkage exerted by the surrounding skin. The transverse elongation λ_T is therefore limited and may not reach $1/\sqrt{\lambda_L}$ corresponding to the incompressibility condition.

For VOI#3 where a volume loss was observed at the spherulitic scale, the "over-contraction" is attributed to the above-mentioned collapse of cylindrical cavities, once the height is large enough, in addition to the Poisson and skin shrinkage cumulative effects (see for VOI#1 and VOI#2). At this stage, see Figure 6(b), the so-called "fragmentation of crystalline lamellae" due to large longitudinal extension induces thinner and less numerous lamellae. Once the collapse of voids is complete, meaning a closure of the elongated voids, λ_T can no longer evolve.

Note that, in Figure 14 the volume increase of the spherulite is observed to slow down from VOI#1 to VOI#2. It can be attributed to VOI#2 containing spherulites that had already started the process of void collapse.

At the macroscopic scale, the compaction is observed for both skin and core and for all VOIs. However, the skin showed less volume loss than the core, with a constant difference in λ_T of about 0.08 all along the VOIs. At the scale of the core, the contraction is due to that of all the spherulites inside the VOI together with the deformation of the extended leftover matrix. The larger the void, the more the negative volumetric deformation due to their collapse. The volume loss in coarse spherulites is greater than that in small ones.

The skin, composed of much smaller spherulites can deform by the rolling/slipping of these spherulites each other. The "flow" of the skin layer can then be attributed essentially to shear without voiding phenomenon. Therefore, the skin shrinks less than the core with coarse spherulites. Additionally, the material flow as mentioned above, operates so as to induce warping of the cross-section of the specimen. The measurement being carried out at mid-width, that is, at the minimum thickness of the material, enhances the compaction relative to the given extension. The core material, is subjected to the "over-contraction" of the skin together with partial collapse of voids inside.

5.2 Consequence on the true strain and true stress

The concept of RVE considers homogeneity of the continuum medium as well as the stress and strain tensors within. While the RVE at the macroscopic scale (skin and core) were described in Section 3.2, that of the spherulite is to be defined. Actually, this RVE was assumed to be that of the core composed of several spherulites, where the average elongations were measured.

The above results, available in the necked region specific to irreversible deformation, highlighted many kinds of heterogeneity:

- longitudinal due to the thickness/width variation along the z-position of the spherulite RVE;
- lateral due to: i) the skin-core effects; ii) the gradient of void volume fraction where the maximum is located in the centre.

In Figures 12 and 13(b), the plastic deformation gradient of the spherulitic RVE can be written using $\lambda_r = \lambda_\theta = \lambda_T$ and $\lambda_z = \lambda_L$. Therefore, for each VOI,

$$\underset{\sim}{F}^{\mathrm{p}} = \begin{pmatrix} \lambda_T^{\mathrm{p}} & 0 & 0 \\ 0 & \lambda_T^{\mathrm{p}} & 0 \\ 0 & 0 & \lambda_L^{\mathrm{p}} \end{pmatrix} \tag{19}$$

was completely obtained. The true plastic strain tensor from Equation (7) is fully determined as

$$\underset{\sim}{\varepsilon}^{\mathrm{p}} = \begin{pmatrix} \ln(J^{-1/3}\lambda_T^{\mathrm{p}}) & 0 & 0 \\ 0 & \ln(J^{-1/3}\lambda_T^{\mathrm{p}}) & 0 \\ 0 & 0 & \ln(J^{-1/3}\lambda_L^{\mathrm{p}}) \end{pmatrix} + \begin{pmatrix} \ln(J^{\mathrm{p}}) & 0 & 0 \\ 0 & \ln(J^{\mathrm{p}}) & 0 \\ 0 & 0 & \ln(J^{\mathrm{p}}) \end{pmatrix} \tag{20}$$

with $J^{\mathrm{p}} = (V/V_0)^{\mathrm{p}} = \lambda_L^{\mathrm{p}}(\lambda_T^{\mathrm{p}})^2$.

This complete true strain tensor, determined experimentally, constituted one of the main results of this work at the spherulitic scale. Equation (20) shows that the strain tensor was split into its deviatoric and volumetric parts respectively. The volumetric strain, called also "plastic dilation" (Ognedal et al. 2014) in the sense that it is irreversible, can be essentially related to the void growth. This latter was quantified in (Laiarinandrasana, Selles, et al. 2016) for the same sample. The complementary deviatoric part represents the shear strain exerted on the matrix.

Focusing on the volumetric part, Figure 14 clearly shows that apart from VOI#1 and VOI#2 at the spherulite scale, the other VOIs exhibited negative volumetric strain in the tensile direction. This compaction i.e. $\nu > 0.5$ cannot be apprehended by classical continuum mechanics. Therefore, these cases will not be further discussed. The deformation gradient or strain tensors for the two selected VOIs can be considered as the inputs to obtain the complete stress tensors. Two approaches can then be identified so as to apply continuum mechanics:

- an average spherulite considered as a homogenised porous medium, the cross-section being that of the core VOI;
- a spherulite consisting of a mix of ideally dense matrix containing an amount of pores which can be converted to void volume fraction (porosity).

In both approaches, as the deformation gradient is not ruled by the incompressibility constraint, the stress tensor is expected to be triaxial: the transverse stresses are not null. Due to the gradients and the 3D effects, only constitutive models relating the strain tensor to the stress tensor, should be utilised. The use of a finite element (FE) code provided with a reliable model is then recommended. Thanks to the measured load, the only known stress is the axial component of the first Piola-Kirchhoff (engineering) stress tensor $\underset{\sim}{\Pi}$:

$$\Pi_L = \frac{F}{S_0} \tag{21}$$

where F is the load, S_0 is the initial area of the cross-section of the core RVE. The experimental results required constitutive models which handle the hydrostatic pressure (isostatic stress) with respect to the volume change. Note that a "simple" von Mises criterion fails to account for this phenomenon. Once the appropriate model is identified, the optimisation of material parameters is based on F/S_0 value so as to calibrate the simulated Π_L.

Π_T can then be accessed, but it depends on the sensitivity of the model to the stress triaxiality *i.e.* the isostatic stress. By returning to Equation (16), the Cauchy (true) stress tensor $\underset{\sim}{\sigma} = \underset{\sim}{\Pi}\,\underset{\sim}{F}^{\top}/J$ can be deduced, yielding

$$\underset{\sim}{\sigma} = \begin{pmatrix} \frac{\Pi_T}{\lambda_L\lambda_T} & 0 & 0 \\ 0 & \frac{\Pi_T}{\lambda_L\lambda_T} & 0 \\ 0 & 0 & \frac{\Pi_L}{\lambda_T^2} \end{pmatrix}. \tag{22}$$

Before the yield stress, that is in the (visco)elastic part of the stress-strain curve, both macroscopic and spherulitic RVEs fulfil the conditions of homogeneity. However, attention should be paid to the use of the true stress σ_L and the true strain $\ln(\lambda_L)$ to derive the elastic coefficients such as Young's modulus or the Poisson's ratio. Beyond the yield stress *i.e.* during the necking process, depending on the chosen model, the true stress-strain curve should be plotted using the maximum principal stress σ_L in Equation (22). Attention should be paid to the transverse stresses which are not null, in contrast to the uniaxial case assumed in the classical stress-strain curve. These investigations are required when working on the local true stresses at the scale of the spherulites.

5.3 Towards AI analysis: machine learning of deformed spherulite morphology

In this work, Figures 6 and 7 allowed the recognition of the shape and the mechanisms of voiding within several spherulites. The top and side views of these spherulites were utilised so as to learn about the characteristic patterns when they were deformed and voided.

The knowledge of the patterns enabled the deformed spherulites in Figures 8 and 9 to be identified, followed by the plotting of the histograms in Figures 10 and 11. All these time-consuming operations were executed by eyes and by hand. The numbers of analysed spherulites are specified in Figures 10 and 11: about 50 and 300 in the side and top views, respectively. These numbers were of course fewer than the total number of spherulites in the tomography data sets.

From the authors' viewpoint, these valuable data could be further exploited. One of the aim of this paper was to give a route for a machine learning approach. The first task consisting of the identification the spherulite patterns in fully 3D, has been detailed in this paper. Based on this knowledge, a machine learning routine should allow the production of more elements in the histograms from big data sets. Furthermore, other spherulitic microstructures coming from other thermoplastics are available in our laboratory to do so.

6 Conclusion

This work focused on an isotactic polypropylene: a semi-crystalline thermoplastic with spherulitic microstructure that exhibited skin-core effects. Three experimental volumes of interest (VOI) were introduced:

- the skin VOI including the free surface, where common laboratory measurements could be carried out;
- the core VOI where the cross-section remained rectangular during the deformation and within which several spherulites could be observed in their deformation process;
- the VOI at the spherulitic scale constituted by the same core VOI but where the evolution of characteristic lengths of the spherulites could be measured all along the shape of the necked region.

For each of the three VOIs, an attempt was made to determine the complete deformation gradient tensor composed of both isochoric and volumetric components. Attention was especially paid to the transverse elongation so as to analyse the volume change. None of the VOIs showed the commonly admitted isochoric assumption, corresponding to the quasi-incompressibility constraint. In contrast, most of them turned out to exhibit volume loss (compaction) of the material at an advanced stage of the necking process. Only two VOIs, located in the neck shoulder (equivalent to the beginning of the necking process during a tensile test) showed a volume increase. This latter was ascribed to void nucleation due to the architecture of the spherulites. The consecutive growth of these voids arranged in columns (polar fans) was then shown when the necking process progressed. The compaction of the VOI was attributed to the collapse of extended cylindrical shaped voids in the deformed polar fans. Thanks to the measurements of average changes in the height and diameter of the spherulites, the complete deformation gradient of the VOIs could be determined beyond the yield stress. Especially the volume increase at the beginning of the necking process made the classical "isochoric" plasticity theory questionable. Therefore, a route was proposed to obtain the local true stress tensor in the framework of continuum mechanics under finite strain formulation. The plastic dilation was accounted for in such modelling dedicated for finite element analysis.

References

Addiego, F., A. Dahoun, C. G'Sell, and J.-M. Hiver (2006). Characterization of volume strain at large deformation under uniaxial tension in high-density polyethylene. *Polymer* 47(12):4387–4399. [DOI], [HAL].

Assouline, E., E. Wachtel, S. Grigull, A. Lustiger, H. Wagner, and G. Marom (2001). Lamellar twisting in α isotactic polypropylene transcrystallinity investigated by synchrotron microbeam X-ray diffraction. *Polymer* 42(14):6231–6237. [DOI], [HAL].

Blaise, A., C. Baravian, S. André, J. Dillet, L. J. Michot, and R. Mokso (2010). Investigation of the mesostructure of a mechanically deformed HDPE by synchrotron microtomography. *Macromolecules* 43(19):8143–8152. [DOI], [HAL].

Cangemi, L., S. Elkoun, C. G'Sell, and Y. Meimon (2004). Volume strain shanges of plasticized Poly(vinylidenefluoride) during tensile and creep Tests. *Journal of Applied Polymer Science* 91(3):1784–1791. [DOI], [HAL].

Duffo, P., B. Monasse, J.-M. Haudin, C. G'Sell, and A. Dahoun (1995). Rheology of polypropylene in the solid state. *Journal of Materials Science* 30(3):701–711. [DOI].

Estevez, R., M. Tijssens, and E. Van der Giessen (2000). Modeling of the competition between shear yielding and crazing in glassy polymers. *Journal of the Mechanics and Physics of Solids* 48(12):2585–2617. [DOI], [OA].

Gaucher-Miri, V., C. Depecker, and R. Séguéla (1997). Reversible strain-induced order in the amorphous phase of a low-density ethylene/butene copolymer. *Journal of Polymer Science Part B: Polymer Physics* 35(13):2151–2159. [DOI], [HAL].

Haudin, J.-M. (2013). Crystallization in processing conditions. Ed. by E. Piorkowska and G. C. Rutledge. Wiley, pp 433–462. [DOI], [HAL].

Kantz, M. R., H. D. Newman, and F. H. Stigale (1972). The skin-core morphology and structure–property relationships in injection-molded polypropylene. *Journal of Applied Polymer Science* 16(5):1249–1260. [DOI].

Laiarinandrasana, L., O. Klinkova, F. Nguyen, H. Proudhon, T. F. Morgeneyer, and W. Ludwig (2016). Three dimensional quantification of the anisotropic void evolution in deformed semi-crystalline Polyamide 6. *International Journal of Plasticity* 83:19–36. [DOI], [HAL].

Laiarinandrasana, L., N. Selles, O. Klinkova, T. F. Morgeneyer, H. Proudhon, and L. Helfen (2016). Structural versus microstructural evolution of semi-crystalline polymers during necking under tension: Influence of the skin-core effects, the relative humidity and the strain rate. *Polymer Testing* 55:297–309. [DOI], [HAL].

Morgeneyer, T. F., H. Proudhon, P. Cloetens, W. Ludwig, Q. Roirand, L. Laiarinandrasana, and E. Maire (2014). Nanovoid morphology and distribution in deformed HDPE studied by magnified synchrotron radiation holotomography. *Polymer* 55(25):6439–6443. [DOI], [HAL].

Ognedal, A. S., A. H. Clausen, A. Dahlen, and O. S. Hopperstad (2014). Behavior of PVC and HDPE under highly triaxial stress states: An experimental and numerical study. *Mechanics of Materials* 72:94–108. [DOI], [OA].

Ovalle, C., P. Cloetens, H. Proudhon, T. F. Morgeneyer, and L. Laiarinandrasana (2021). Nanocavitation mechanisms in deformed High Density PolyEthylene (HDPE) using synchrotron radiation NanoTomography. *Polymer* 229:123959. [DOI], [OA].

Pawlak, A. and A. Galeski (2008). Cavitation during tensile deformation of polypropylene. *Macromolecules* 41(8):2839–2851. [DOI].

Pawlak, A. and A. Galeski (2010). Cavitation and morphological changes in Polypropylene deformed at elevated temperatures. *Journal of Polymer Science Part B: Polymer Physics* 48(12):1271–1280. [DOI], [OA].

Ponçot, M., F. Addiego, and A. Dahoun (2013). True intrinsic mechanical behaviour of semi-crystalline and amorphous polymers: Influences of volume deformation and cavities shape. *International Journal of Plasticity* 40:126–139. [DOI], [HAL].

Raphael, I., N. Saintier, G. Robert, J. Béga, and L. Laiarinandrasana (2019). On the role of the spherulitic microstructure in fatigue damage of pure polymer and glass-fiber reinforced semi-crystalline polyamide 6.6. *International Journal of Fatigue* 126:44–54. [DOI], [OA].

Rozanski, A. and A. Galeski (2013). Plastic yielding of semicrystalline polymers affected by amorphous phase. *International Journal of Plasticity* 41:14–29. [DOI].

Séguéla, R. (2007). On the natural draw ratio of semi-crystalline polymers: Review of the mechanical, physical and molecular aspects. *Macromolecular Materials and Engineering* 292(3):235–244. [DOI], [HAL].

Selles, N., P. Cloetens, H. Proudhon, T. F. Morgeneyer, O. Klinkova, N. Saintier, and L. Laiarinandrasana (2017). Voiding mechanisms in deformed polyamide 6 observed at the nanometric scale. *Macromolecules* 50(11):4372–4383. [DOI], [HAL].

van Dommelen, J. A. W., D. M. Parks, M. C. Boyce, W. A. M. Brekelmans, and F. P. T. Baaijens

(2003). Micromechanical modeling of the elasto-viscoplastic behavior of semi-crystalline polymers. *Journal of the Mechanics and Physics of Solids* 51(3):519–541. [DOI].

Ward, I. M. (1971). Review: The yield behaviour of polymers. *Journal of Materials Science* 6(11):1397–1417. [DOI].

Xiong, B., O. Lame, J. Chenal, C. Rochas, R. Séguéla, and G. Vigier (2013). In-situ SAXS study and modeling of cavitation/crystal-shear competition in semi-crystalline polymers: influence of temperature and microstructure in polyethylene. *Polymer* 54(20):5408–5418. [DOI], [HAL].

Xiong, B., O. Lame, R. Séguéla, and Y. Men (2018). Micro/macro-stress relationship and local stress distribution in polyethylene spherulites upon uniaxial stretching in the small strain domain. *Polymer* 140:215–224. [DOI], [HAL].

Open Access This article is licensed under a Creative Commons Attribution 4.0 International License, which permits use, sharing, adaptation, distribution and reproduction in any medium or format, as long as you give appropriate credit to the original author(s) and the source, provide a link to the Creative Commons license, and indicate if changes were made. The images or other third party material in this article are included in the article's Creative Commons license, unless indicated otherwise in a credit line to the material. If material is not included in the article's Creative Commons license and your intended use is not permitted by statutory regulation or exceeds the permitted use, you will need to obtain permission directly from the authors–the copyright holder. To view a copy of this license, visit creativecommons.org/licenses/by/4.0.

Authors' contributions LL: conceptualization, supervision, writing - original draft, review & editing. OK: formal analysis, visualization. CO: validation, formal analysis, visualization, writing - review & editing. PC: investigation, methodology, visualization. HP: investigation, methodology, visualization. TFM: investigation, methodology, visualization, writing - review & editing.

Supplementary Material Experimental datasets and high-quality images used in the paper are available at the permalink 10.5281/zenodo.13788675.

Acknowledgements The authors would like to acknowledge the European Synchrotron Radiation Facility (ESRF) in Grenoble, France: (i) Beamline ID22 for experiment MA1647; (ii) Beamline ID19, and especially Lukas Helfen, for experiment MA1276.

Competing interests The authors declare that they have no competing interests.

Journal's Note JTCAM remains neutral with regard to the content of the publication and institutional affiliations.